The Kerr Metric and the Quest for Sharper Shadows

Mayukh Bagchi
Queen's University
mayukh.bagchi@queensu.ca

June 9, 2024

Abstract

Astrophysical black holes arise from the remnants of massive stars, typically those exceeding $20M_{\odot}$. When these stars exhaust their nuclear fuel, they explode as supernovae. The core then collapses under gravitational forces. If the mass surpasses approximately $3M_{\odot}$, no force can stop the contraction, creating a singularity encased by an event horizon. Given the conservation of angular momentum, these black holes usually rotate, making the Kerr metric (Kerr, 1963), which describes spacetime around rotating masses, more applicable than the Schwarzschild solution for non-rotating black holes.

Recent advancements in radio instrumentation have allowed us to directly image the shadow of distant supermassive black holes. Very Long Baseline Interferometry (VLBI) employs continental baselines, integrating premier mm/sub-mm radio telescopes to image remote objects. The Event Horizon Telescope (EHT) notably utilized this technique to capture the shadows of the black holes M87* (Collaboration et al., 2019) and Sag A* (Akiyama et al., 2022), achieving remarkable resolution. However, at the current 230 GHz range, the maximum angular resolution is approximately 22 μas, constrained by Earth's diameter. To enhance our resolution, observations at higher frequencies in the sub-mm are necessary, but Earth's atmosphere restricts these frequencies from most locations. Higher-resolution observations would not only enable us to discern more distant black holes but also their photon rings, offering a route to precise black hole property measurements and Kerr metric validations.

This report will outline the formation of astrophysical black holes, elucidate the Kerr Metric's general relativistic aspects, and describe particle trajectories in such rotating systems. All the analyses for the Kerr geometry have been carried out in `Python` using the `EinsteinPy` library (EinsteinPy Development Team, 2024) which is an open-source package dedicated to problems arising in General Relativity and gravitational physics. It will then present the EHT collaboration's findings on black hole shadows and conclude with future EHT prospects and the potential of balloon and space-based interferometers for increasing resolution.

1 Introduction

1.1 Astrophysical black holes

The formation of astrophysical black holes, celestial objects of such extreme density that nothing, not even light, can escape their gravitational pull, is a subject that captures

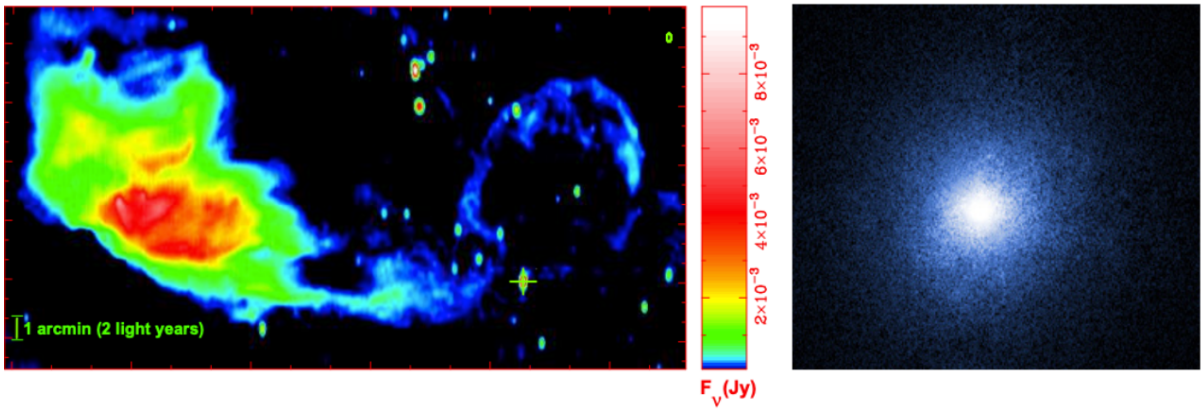

Figure 1: First panel showing a highly collimated relativistic jet at 1.4 GHz around a Galactic stellar black hole from Cygnus X-1 region (Gallo et al., 2005). The second panel shows a Chandra X-ray image of the same region (Miller, 2007).

the intersection of theoretical speculation and observational astronomy. The conceptual journey begins with the Newtonian mechanics' proposition by John Michell in 1783 and independently by Pierre-Simon Laplace in 1796, theorizing the existence of "dark stars" whose escape velocity surpasses the speed of light. These musings laid the groundwork for what would, centuries later, be recognized as black holes. The equation is given by,

$$R = \frac{2GM}{c^2} \tag{1}$$

where R marks the radius beneath which the escape velocity exceeds the speed of light, encapsulating this early theoretical foundation. Where M is the object mass, G is the gravitational constant, and c is the speed of light.

The formalism of black holes, however, owes its rigor to the 20th-century advent of general relativity (Einstein et al., 1916). This was followed by Karl Schwarzschild's discovery of the Schwarzschild solution, describing the spacetime around a non-rotating, spherically symmetric black hole. Subsequent solutions, including the Kerr solution for rotating black holes, further elaborated the mathematical underpinning of these objects, encapsulating their properties solely in terms of mass (M), spin angular momentum (J), and, theoretically, electric charge (Q), though the latter is negligible for astrophysical objects.

Astrophysical observations as referred in Fig 1 have corroborated the theoretical existence of black holes, beginning with the dynamical measurement of the compact object in Cygnus X-1 in the early 1970s. This period heralded the search for black holes in the universe, employing techniques to measure the masses and spins of these enigmatic objects. Notably, the equation defining the gravitational radius,

$$r_g = \frac{GM}{c^2} = 14.77 \frac{M}{10M_\odot} \text{km} \tag{2}$$

where $M_\odot$ denotes the mass of the Sun, and highlights the scale at which black hole effects become significant. The discovery of gravitational waves by LIGO in 2015 from the merger of two black holes, and the first image of a black hole (Fig 2) by the Event Horizon Telescope in 2019, underscore the empirical foundations supporting black hole physics.

Figure 2: First-ever image of a black hole shadow at the center of Galaxy M87 (Collaboration et al., 2019). The image shows a bright ring formed as light bends in the intense gravity around a black hole that is 6.5 billion times more massive than the Sun.

The theoretical exploration and empirical investigation into black holes provide a profound understanding of these cosmic phenomena. The interplay between general relativity and observations across the electromagnetic spectrum, from radio to X-rays, enables the study of black holes from stellar mass to supermassive scales. This symbiosis of theory and observation not only enriches our understanding of the universe but also serves as a testament to the predictive power of physical laws over the vast expanse of cosmic scales.

1.2 VLBI and Imaging Black Holes

Very Long Baseline Interferometry (VLBI) enables the synthesis of Earth-sized virtual telescopes, achieving angular resolutions sharp enough to observe the photon rings of supermassive black holes (SMBHs) like M87* and Sgr A*. By combining signals from dispersed telescopes, VLBI overcomes the diffraction limit, crucial for imaging black holes at their event horizons. However, millimeter-wavelength VLBI faces challenges such as limited antenna receiver sensitivity and short atmospheric coherence times, which are mitigated by technological advancements and the integration of powerful telescopes like ALMA into the Event Horizon Telescope (EHT) array.

The EHT's images of M87* and Sgr A* have provided unprecedented evidence of black hole shadows and photon rings, marking a significant milestone in astrophysics. These images validate general relativity's predictions and offer insights into the dynamics near black holes.

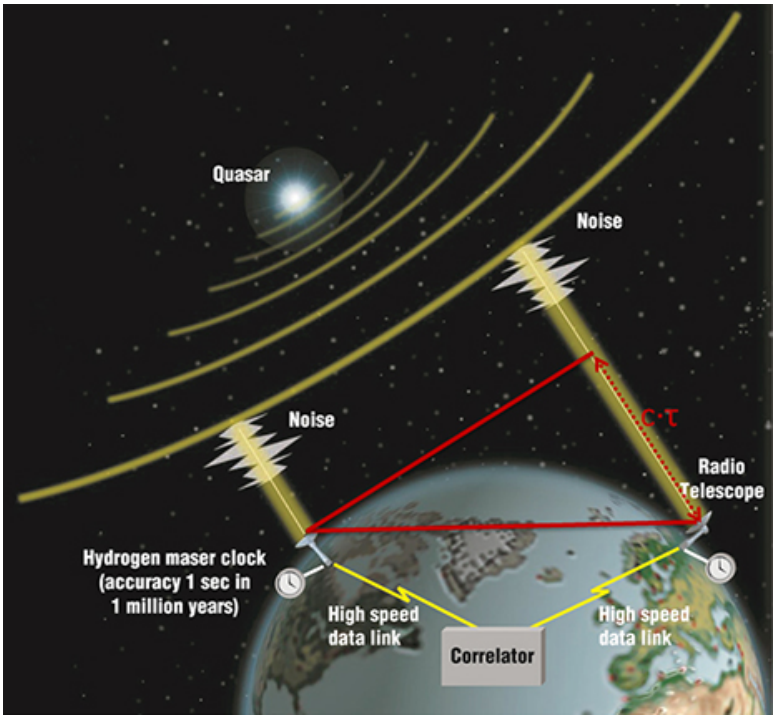

Figure 3: A cartoon explaining how VLBI works. Unlike traditional interferometry, VLBI uses continental baselines in order to improve the angular resolution of the observations relying on highly stable hydrogen masers to timestamp the raw signals. The signals recorded in physical drives are then brought to a central facility and correlated.

2 The Kerr Metric and orbits around rotating Black Holes

2.1 The Kerr Spacetime

The Kerr geometry, discovered by Roy Kerr in 1963, extends the Schwarzschild solution to include rotating black holes, characterized by mass M and angular momentum J. This geometry is pivotal in understanding the most general rotating black-hole solutions in vacuum spacetime as described by general relativity. Unlike the non-rotating Schwarzschild black holes, Kerr black holes are defined by two parameters: the mass M and the Kerr parameter a, where $a \equiv J/M$, representing the black hole's angular momentum per unit mass.

The Kerr metric in Boyer-Lindquist coordinates (t, r, θ, ϕ), a generalization of Schwarzschild coordinates, is given by:

$$\begin{aligned} ds^2 = &- \left(1 - \frac{2Mr}{\rho^2}\right) dt^2 - \frac{4Mar\sin^2\theta}{\rho^2} d\phi dt + \frac{\rho^2}{\Delta} dr^2 \\ &+ \rho^2 d\theta^2 + \left(r^2 + a^2 + \frac{2Mra^2\sin^2\theta}{\rho^2}\right) \sin^2\theta d\phi^2 \end{aligned} \tag{3}$$

where $a \equiv J/M$, $\Delta \equiv r^2 - 2Mr + a^2$ and $\rho^2 \equiv r^2 + a^2\cos^2\theta$. This metric encapsulates the spacetime surrounding a rotating black hole, demonstrating significant properties including asymptotic flatness, stationarity, and axisymmetry. The Kerr geometry ap-

proaches the geometry of flat spacetime far from the black hole, establishing that the spacetime curvature induced by the black hole can be attributed to its mass M and angular momentum J.

The metric as shown in Eq. 3 is a solution of the vacuum Einstein equation. Various significant attributes of the Kerr geometry can be directly derived from this particular metric expression.

1. **Asymptotically Flat**: The Kerr metric simplifies notably when considering a region far from the black hole, where the radial distance r is much larger than both the black hole's mass M and its angular momentum per unit mass a. In this regime, the line element approximates to,

$$ds^2 \approx -\left(1 - \frac{2M}{r}\right) dt^2 + \left(1 + \frac{2M}{r}\right) dr^2 + r^2(d\theta^2 + \sin^2\theta d\phi^2) - \frac{4Ma}{r^2} \sin^2\theta (r d\phi) dt + \ldots, \tag{4}$$

   This form indicates that at large distances, the Kerr spacetime behaves as though it is flat, mirroring the spacetime far from a massive body. The leading terms in each metric coefficient reveal this behavior, with the inverse radius corrections kept where applicable. From such a distance, the curvature of spacetime attributed to the black hole can be inferred from the movement of satellites in distant orbits, as their paths are influenced by the black hole's mass. Additionally, the precession of orbiting gyroscopes can give away the black hole's angular momentum.

2. **Killing Vectors** : The Kerr metric exhibits time-independence and rotational symmetry, being constant in both time (t) and the azimuthal angle (ϕ). These features are embodied by two Killing vectors:

$$\xi^\alpha = (1, 0, 0, 0) \qquad \text{(Time-independent, stationary)} \tag{5}$$
$$\eta^\alpha = (0, 0, 0, 1) \qquad \text{(axisymmetric)} \tag{6}$$

   These vectors demonstrate the invariance of the metric under time translations and rotations around the axis of symmetry. Furthermore, the Kerr metric remains the same upon a reflection across the equatorial plane, indicated by $\theta = \pi/2$, where it sends θ to $\pi - \theta$, a reflective symmetry characteristic of the spacetime surrounding a rotating mass. Despite these symmetries, it's notable that the Kerr spacetime does not possess spherical symmetry. This is evidenced by the dependence of the metric coefficients g_{tt} and g_{rr} on the polar angle θ, highlighting the anisotropic nature of the geometry due to the central object's rotation.

3. **Non-rotating case**: In the absence of rotation, when the Kerr parameter a is set to zero, the Kerr metric as mentioned in Eq 3 transitions to the Schwarzschild metric, as expressed in Schwarzschild coordinates. This reveals that the family of Kerr solutions encompasses the Schwarzschild solution as a particular instance where the black hole has no angular momentum.

   For a non-rotating black hole, where the spin parameter $a = 0$, the Kerr metric simplifies as follows:

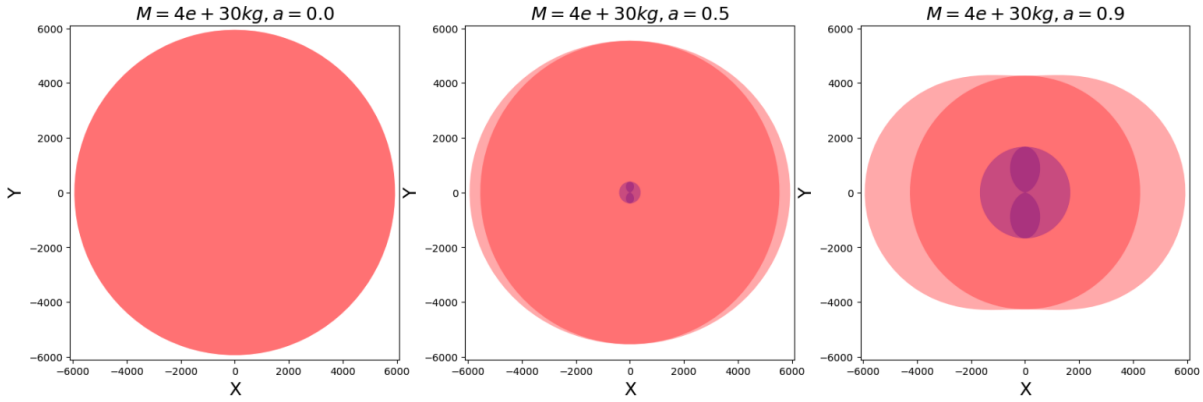

Figure 4: A plot showing a 4×10^{30} kg Black Hole with different spin parameters a. The surfaces are clearly visible in the plots. Going radially inward, we have Outer Ergosphere, Outer Event Horizon, Inner Event Horizon and Inner Ergosphere. We can also observe that as the spin parameter $a \to 1$ (its maximum attainable value), the individual singularities become prominent. On the other hand as $a \to 0$ some singularities appear to fade away, leaving us with a single surface, that is the Event Horizon of a Schwarzschild black hole.

- The term ρ^2 simplifies to r^2.
- The term Δ simplifies to $r^2 - 2Mr$.
- The cross-term involving $d\phi dt$ vanishes.
- The coefficient of $d\phi^2$ simplifies significantly.

Thus, the Kerr metric reduces to the Schwarzschild metric:

$$ds^2 = -\left(1 - \frac{2M}{r}\right) dt^2 + \frac{dr^2}{1 - \frac{2M}{r}} + r^2 d\theta^2 + r^2 \sin^2\theta d\phi^2, \tag{7}$$

which describes the spacetime around a non-rotating, spherically symmetric mass.

4. **Singularities and Horizon**: The Kerr metric is characterized by singularities that emerge when the function ρ is null and the quantity Δ vanishes as shown in Fig 4. Specifically, a real singularity—indicative of infinite spacetime curvature—occurs at the coordinates $r = 0$ and $\theta = \frac{\pi}{2}$. This singularity aligns with that of the Schwarzschild geometry's singular point at $r = 0$, when the rotation parameter a is set to zero.

   The expression for Δ is given by:

$$\Delta = r^2 - 2Mr + a^2 \tag{8}$$

   and becomes zero at radii $r_\pm = M \pm \sqrt{M^2 - a^2}$, which are identified as coordinate singularities. Such singularities can typically be removed by transitioning to an alternate coordinate system. The radius r_+ aligns with the Schwarzschild radius at $2M$ when $a = 0$ and marks the Kerr black hole's event horizon, which cloaks the real singularity from an external viewpoint.

   The Kerr spacetime inside the horizon, particularly for $r < r_+$ (e.g., at $r = r_-$), reveals a complex and rich structure. Nevertheless, astrophysical studies predominantly concentrate on the spacetime properties exterior to the event horizon, due

to their significant implications for observational astronomy and theoretical astrophysics.

2.2 Event Horizon of a Kerr Black Hole

The horizon of a black hole is described as the ultimate boundary from which light cannot escape, forming a null three-surface. For Schwarzschild black holes, this surface is at a constant radius of $r = 2M$. Light can escape from any point outside this horizon, but none can from inside it. The horizon serves as the demarcation line that segregates the region of spacetime that is causally disconnected from an external observer.

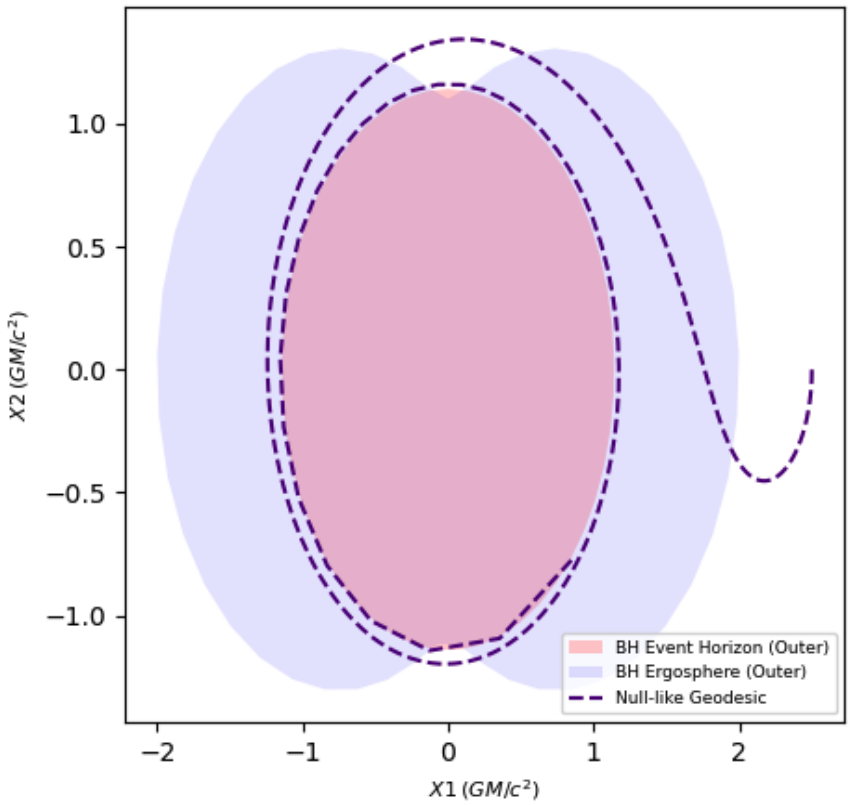

Figure 5: A plot showing a Kerr black hole's event horizon and the ergosphere. The plot shows that the photon's trajectory is reversed due to frame-dragging effects, so that it moves in the direction of the black hole's spin, before eventually falling into the black hole.

The boundary of the region from which light can escape a black hole is a three-surface created by light rays that are in a delicate balance between falling into the black hole and escaping to infinity. This surface termed the horizon, is a null three-surface, where each point has a null tangent vector that is orthogonal to two spacelike tangent vectors. This null surface is stationary and axisymmetric, matching the symmetries of a rotating black hole. The horizon is formed by the light rays that remain at a constant radius, suggesting that these light rays neither move outward towards infinity nor inward towards the black hole's center, maintaining a stable position in the black hole's gravitational field.

The horizon of a Kerr black hole, specifically denoted as $r = r_+$, is characterized as a stationary, axisymmetric null surface within the Kerr geometry. To illustrate that $r = r_+$

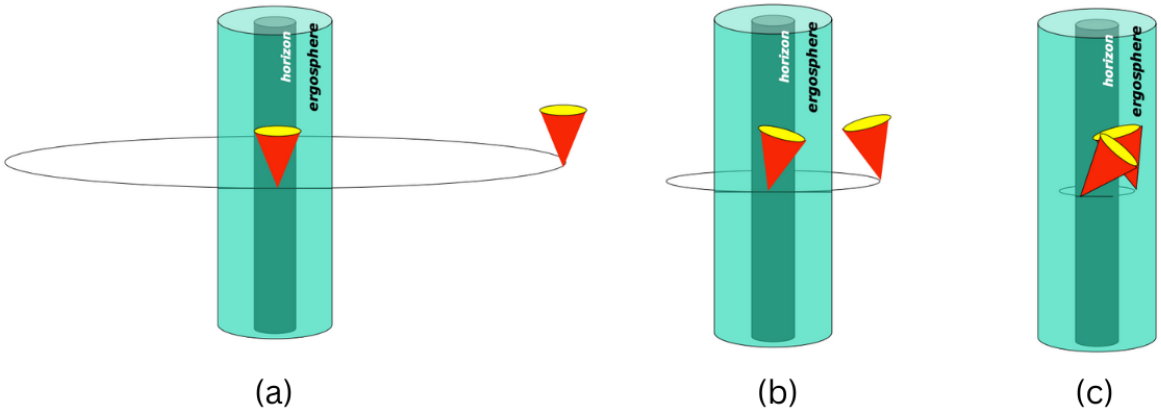

Figure 6: A cartoon illustrating the light cone structure around a rotating black hole. The first image (a) shows a spacetime diagram of light cones orbiting around a Kerr black hole. The second image (b) shows the orbits of the light cones as they get closer to the black hole. The tilt in the light cones is due to the effect of frame dragging. Finally, the third image (c) shows that within the ergosphere, light cones are even more tipped such that all futures rotate in the sense of a black hole. In other words, within the ergosphere it is impossible to stand still.

is indeed a null surface, one can examine its tangent vectors t^α. These vectors lie within the constant r surface and have the form $t^\alpha = (t^t, 0, t^\theta, t^\phi)$.

The condition for a null surface can be satisfied when the dot product of the null vector $\ell \cdot \ell = 0$. In the Kerr metric in Boyer-Lindquist coordinates, the condition $\ell \cdot \ell = 0$ for a tangent vector of the form (15.7) simplifies to:

$$\left(\frac{2Mr_+ \sin\theta}{\rho_+}\right)^2 (\ell^\phi)^2 - \frac{a}{2Mr_+}(\ell^t)^2 + \rho_+^2 (\ell^\theta)^2 = 0 \tag{9}$$

Here, ρ_+ represents ρ evaluated at r_+. The only solution to this equation for $\ell^\theta = 0$ and $\ell^\phi = \frac{a}{2Mr_+}\ell^t$. This leads to the unique null vector in the $r = r_+$ three-surface being expressed as:

$$\ell^\alpha = (1, 0, 0, \Omega_H) \tag{10}$$

where Ω_H is the angular velocity of the black hole's horizon, defined by the equation:

$$\Omega_H = \frac{a}{2Mr_+} \tag{11}$$

This angular velocity is an essential feature of the Kerr black hole, indicating that the horizon itself is rotating, a manifestation of the spacetime-dragging effect induced by the black hole's rotation.

2.3 Orbits and Effective Potential

In the equatorial plane of Kerr geometry, the dynamics of test particles and light rays diverge significantly from their Schwarzschild counterparts due to the absence of spherical symmetry, preserving only axial symmetry.

The governing metric for equatorial orbits, limited to $\theta = \frac{\pi}{2}$, is given by

$$ds^2 = -\left(1 - \frac{2M}{r}\right) dt^2 + \frac{4Ma}{r} dt d\phi + \left(r^2 + a^2 + \frac{2Ma^2}{r}\right) d\phi^2 - \frac{r^2}{\Delta} dr^2 \tag{12}$$

where $\Delta = r^2 - 2Mr + a^2$.

Orbits are characterized by the conserved energy per unit mass e, and angular momentum per unit mass ℓ, stemming from the symmetries of the Kerr metric, expressed as

$$e = -\xi \cdot u, \tag{13}$$

$$\ell = \eta \cdot u. \tag{14}$$

The effective potential for radial motion of particles, $V_{\text{eff}}(r, e, \ell)$, is

$$V_{\text{eff}}(r, e, \ell) = -\frac{M}{r} + \frac{\ell^2 - a^2(e^2 - 1)}{2r^2} - \frac{M(\ell - ae)^2}{r^3}, \tag{15}$$

leading to the radial motion equation

$$e^2 - 1 = \frac{1}{2}\left(\frac{dr}{d\tau}\right)^2 + V_{\text{eff}}(r, e, \ell). \tag{16}$$

For light rays, the effective potential $W_{\text{eff}}(r, b, \sigma)$ depends on the impact parameter $b = \ell/e$ and the co-rotating or counter-rotating nature relative to the black hole's spin:

$$W_{\text{eff}}(r, b, \sigma) = \frac{1}{r^2}\left(1 - \frac{a^2}{b^2}\right) - \frac{2M}{r^3}\left(1 - \sigma\frac{a}{b}\right). \tag{17}$$

The extremal Kerr black hole ($a = M$) features distinctive orbits at $r = 2M$ and $r = 4M$ for co-rotating and counter-rotating photons, indicative of the profound influence of the black hole's rotation on the surrounding spacetime. These equations are indispensable for interpreting astrophysical phenomena, including the mechanisms of energy extraction in the vicinity of rotating black holes.

In Kerr geometry, the study of orbits within the equatorial plane reveals the intricate nature of spacetime around rotating black holes. A particle orbiting at a radius R must have an initial radial velocity of zero for it to maintain a circular orbit. The condition for this stationary orbit, derived from the effective potential, is given by:

$$\frac{e^2 - 1}{2} = V_{\text{eff}}(R, e, \ell) \tag{18}$$

Additionally, the particle must have no radial acceleration:

$$\left.\frac{\partial V_{\text{eff}}(r, e, \ell)}{\partial r}\right|_{r=R} = 0 \tag{19}$$

Stable circular orbits are those where the effective potential is at a minimum:

$$\left.\frac{\partial^2 V_{\text{eff}}(r, e, \ell)}{\partial r^2}\right|_{r=R} > 0 \tag{20}$$

For the innermost stable circular orbit (ISCO), the condition for radial acceleration becomes an equality. Solving the equations for the specific energy e, the specific angular

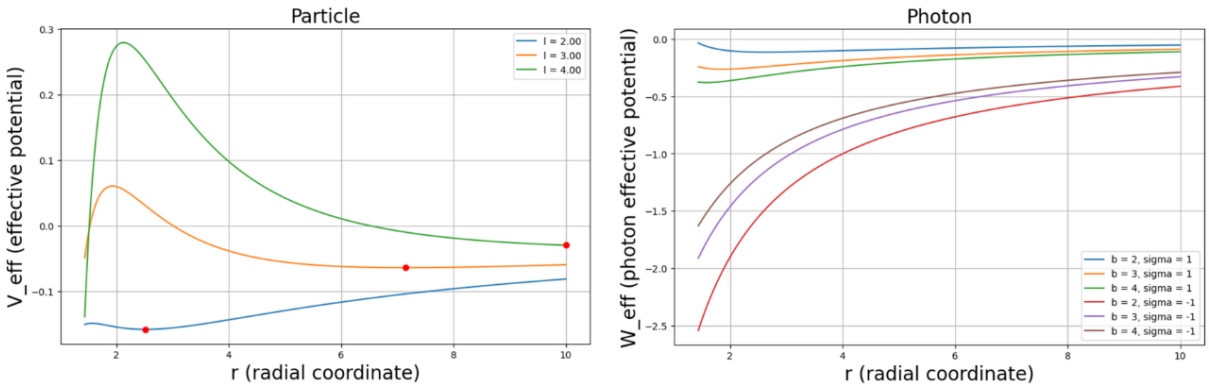

Figure 7: The first figure shows the radial effective potential V_{eff} for different specific angular momenta (ℓ) of test particles in the equatorial plane of a Kerr black hole. The stable orbits have been marked by the red dots on these lines. The black hole's spin a modifies the potential, influencing particle orbits. The second figure is photon effective potential W_{eff} for varying impact parameters (b) and angular momentum orientations (σ) around a Kerr black hole. The plot illustrates the rotation-induced asymmetry in photon orbit potentials.

momentum ℓ, and the radius R yields the parameters for the ISCO. Here, the binding energy per unit rest mass, $1-e$, attains its maximum value. Specifically, in the case of an extremal Kerr black hole, where the spin parameter a equals the mass M, the ISCO and the corresponding maximal fractional binding energy provide critical insights into the black hole's gravitational pull. The parameters for the ISCO in this extremal scenario are as follows:

$$e = \frac{1}{\sqrt{3}}, \quad \ell = \frac{2M}{\sqrt{3}}, \quad r_{\text{ISCO}} = M. \tag{21}$$

In such extremal Kerr black holes, the binding energy can reach approximately 42%. However, for non-extremal Kerr black holes, where the spin-up results from accretion processes, the efficiency of energy release, while still significant, is less than in the extremal case. For these realistic black holes, the maximum a/M ratio is about 0.998, which corresponds to a maximal fractional binding energy of roughly 30%.

The radius of the innermost stable circular orbit (ISCO), denoted as R_{ISCO}, encapsulates the complex interplay between a Kerr black hole's spin and the relativistic dynamics of particles in its vicinity. The relation between R_{ISCO} and the dimensionless spin parameter a/M bifurcates distinctly for corotating and counterrotating orbits due to frame-dragging effects.

Functions Z_1 and Z_2, which are intermediary variables in the expression for R_{ISCO}, are defined as follows:

$$Z_1 = 1 + (1 - a^2/M^2)^{1/3} \left[(1 + a/M)^{1/3} + (1 - a/M)^{1/3}\right] \tag{22}$$

$$Z_2 = \sqrt{3a^2/M^2 + Z_1^2} \tag{23}$$

For *corotating orbits*, where particles move in the same rotational direction as the black hole, R_{ISCO} decreases with an increase in a/M due to the supportive role of the

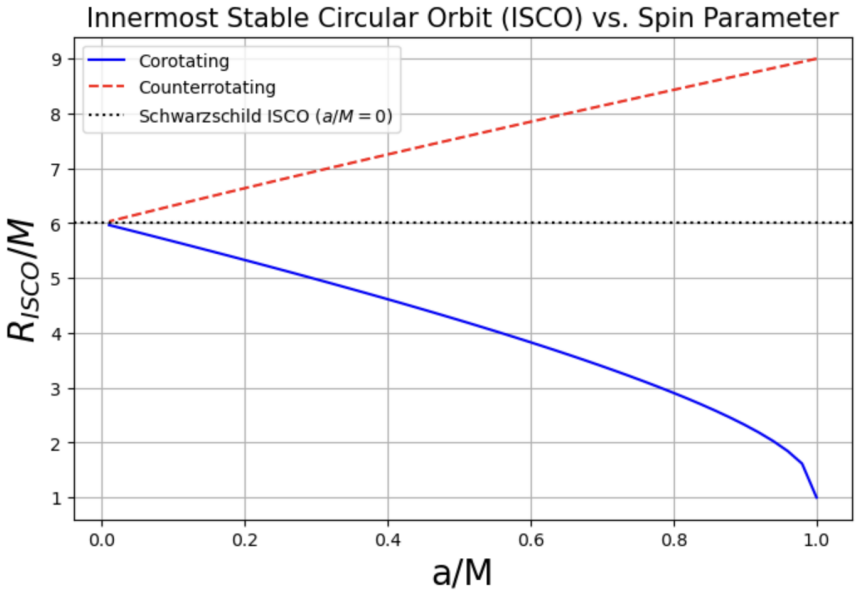

Figure 8: The graph illustrates the variation of R_{ISCO} with the black hole's spin parameter a/M, showing a monotonically decreasing function for corotating orbits and a monotonically increasing function for counterrotating orbits, relative to the non-spinning Schwarzschild case.

black hole's angular momentum:

$$R_{\text{ISCO, corot}}(a) = M\left[3 + Z_2 - \sqrt{(3 - Z_1)(3 + Z_1 + 2Z_2)}\right] \tag{24}$$

Conversely, for *counterrotating orbits*, where particles move in opposition to the black hole's rotation, R_{ISCO} increases with a/M:

$$R_{\text{ISCO, counterrot}}(a) = M\left[3 + Z_2 + \sqrt{(3 - Z_1)(3 + Z_1 + 2Z_2)}\right] \tag{25}$$

In the limit of a non-rotating (Schwarzschild) black hole, where $a = 0$, both corotating and counterrotating orbits converge to the same R_{ISCO} of:

$$R_{\text{ISCO, Schwarzschild}} = 6M \tag{26}$$

The nuanced behavior of R_{ISCO} as a function of the Kerr black hole's spin parameter a/M underscores the pivotal role of the black hole's angular momentum in warping the surrounding spacetime. The effect known as frame-dragging causes spacetime itself to swirl around the rotating mass. Near the event horizon, this phenomenon is particularly pronounced, leading to the dragging of inertial frames in the direction of the black hole's rotation. Such significant alteration in spacetime not only modifies the trajectories of particles and light but also affects the entire accretion process.

For *accretion disk emissions*, the differential rotation of spacetime leads to an asymmetry in the emission profiles. Material spiraling into the black hole at the ISCO moves with velocities close to the speed of light, and due to relativistic beaming, emissions from the disk material moving towards the observer are significantly boosted, while emissions from material moving away are redshifted. This relativistic beaming effect is enhanced for corotating material near the event horizon, contributing to the high luminosity and spectral characteristics observed in X-ray binaries and active galactic nuclei.

2.4 Calculation of Geodesics in Kerr Spacetime

Investigating the dynamics of particles and light in the vicinity of rotating black holes necessitates a thorough understanding of geodesics within Kerr spacetime. The geometry of this spacetime is described by the Kerr metric, which, in Boyer-Lindquist coordinates (t, r, θ, ϕ), is expressed through the line element as shown in Eq 3. Where G is the gravitational constant, M denotes the mass of the black hole, a represents the black hole's angular momentum per unit mass, r is the radial coordinate, θ the polar coordinate, ϕ the azimuthal angle, $\Delta = r^2 - 2GMr + a^2$, and $\rho^2 = r^2 + a^2 \cos^2 \theta$.

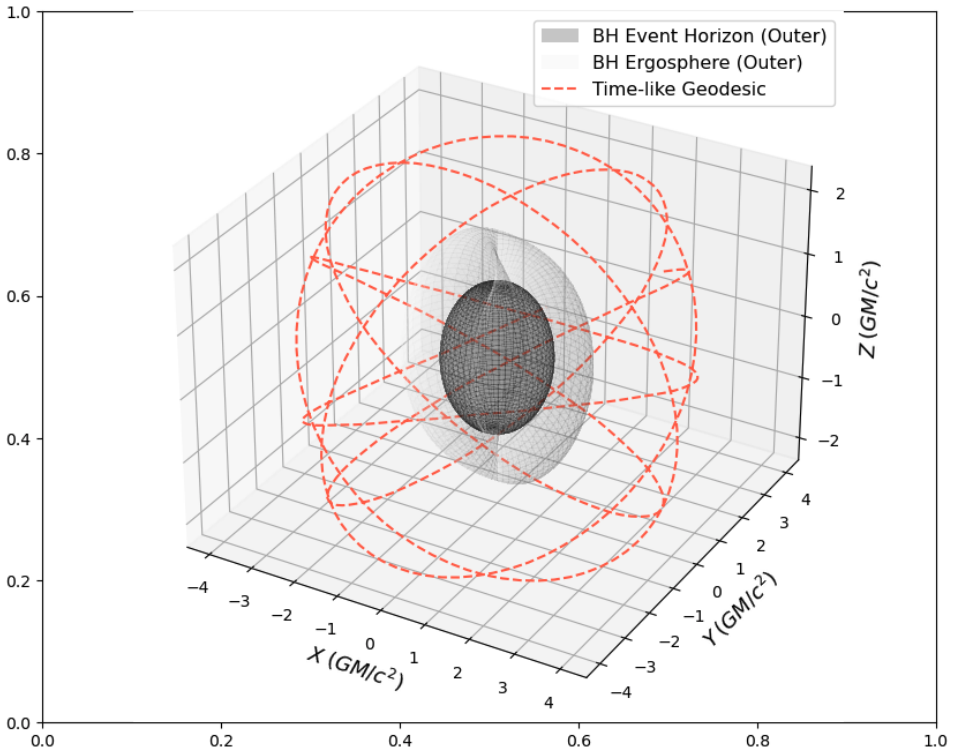

Figure 9: A figure showing the timelike geodesics of a particle around a Kerr black hole simulated using the `EinsteinPy` package. The geodesic has been highlighted in orange color, the black hole event horizon is represented in dark grey, and the ergosphere is represented in light grey color.

The challenge of computing geodesics in such a complex spacetime necessitates the use of the Hamilton-Jacobi formalism, a powerful technique in classical mechanics that extends to general relativity. This approach exploits the separability of the Hamilton-Jacobi equation in Kerr spacetime, which can be written as:

$$\frac{\partial S}{\partial \tau} + \frac{1}{2} g^{\mu\nu} \frac{\partial S}{\partial x^\mu} \frac{\partial S}{\partial x^\nu} = 0, \tag{27}$$

where S denotes Hamilton's principal function, embodying the action of the system. Given the symmetries of the Kerr spacetime, S adopts a separable form:

$$S = -Et + L\phi + S_r(r) + S_\theta(\theta), \tag{28}$$

with E and L being the conserved energy and angular momentum of the test particle, respectively, and $S_r(r)$ and $S_\theta(\theta)$ representing the radial and polar parts of the action, which are functions solely of r and θ.

To solve for geodesics the `EinsteinPy` package was used. `EinsteinPy` first separates the Hamilton-Jacobi equation into partial differential equations by exploiting the metric's symmetries. This separation leads to the identification of conserved quantities along the geodesics, such as the energy E, angular momentum L, and an additional constant known as Carter's constant Q, which arises due to the hidden symmetries of the Kerr spacetime as shown in Sec 2.3. The resulting equations of motion for the test particles or photons are then integrated using numerical techniques. These equations are highly nonlinear and coupled. Numerical integration, employing adaptive step-size Runge-Kutta is used for the computation of geodesic trajectories under a wide range of initial conditions.

3 Black Hole shadows and what do they tell us

The Event Horizon Telescope Collaboration provided groundbreaking empirical evidence of such a shadow in M87*, a supermassive black hole at the center of the galaxy M87 (Akiyama et al., 2022). This finding was facilitated by very long baseline interferometry (VLBI), which could synthesize a telescope array with Earth-spanning diameters, achieving the necessary resolution to detect the shadow at a wavelength of 1.3 mm.

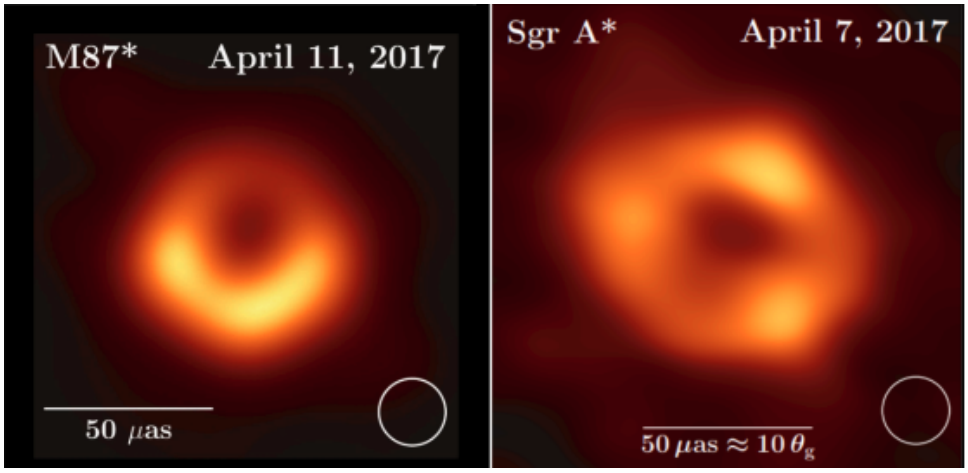

Figure 10: Images of M87* (left) and Sgr A* (right) published by the EHT Collaboration. The angular scales are mentioned at the bottom in white.

The shadow itself, a consequence of gravitational light bending and photon capture at the event horizon, provides a visible confirmation of the black hole's existence and allows the testing of GR in the strong-field regime. The diameter of this shadow can be approximated by $d = \alpha\theta_g$, where α is a dimensionless parameter dependent on the black hole's spin and inclination, $\theta_g = GM/c^2D$ is the angular gravitational radius, M is the black hole mass, G is the gravitational constant, c is the speed of light, and D is the distance to the observer.

The asymmetry in the emission ring's brightness, as detailed by the EHT Collaboration, is attributable to the relativistic beaming of material orbiting close to the speed of light in the strong gravitational field near the black hole (Blandford and Znajek, 1977). This asymmetry gives clues about the black hole's spin direction and the dynamics of accretion processes occurring near the event horizon.

3.1 Properties of M87*

The EHT measured the black hole's shadow diameter as $42 \pm 3\mu as$, which, given the distance of M87 estimated at $16.8 \pm 0.8 Mpc$, yields a mass for M87* of $(6.5 \pm 0.7) \times 10^9 M_\odot$. This observed shadow is consistent with the predicted gravitational silhouette cast by the black hole's event horizon as light bends in the intense gravitational field, described by the Kerr metric of a rotating black hole in General Relativity.

Given the angular diameter of the black hole shadow $\delta = 42\mu as$ and the distance to M87 $D_L = 16.8$ Mpc, we first convert the angular diameter to radians and then to the physical diameter of the shadow:

$$D = 2\delta D_A = 2 \left(\frac{42 \times 10^{-6}}{206265} \right) \left(16.8 \times 10^6 \text{ pc}\right) \left(3.086 \times 10^{16} \text{ m/pc}\right) \tag{29}$$

Given that the shadow diameter is due to the photon sphere in the Kerr metric, we can relate the shadow radius R_s to the black hole mass M through the relation:

$$R_s = \frac{r_{ph}}{\sqrt{1 - \frac{a^2}{r_{ph}^2}}} \tag{30}$$

For non-extreme spin values and assuming an equatorial observer, we approximate $r_{ph} \approx 3M$. The mass M can then be estimated as:

$$M \approx \frac{R_s}{3} \approx \frac{D}{6} \tag{31}$$

Inserting the value of D from equation (1), we find:

$$M \approx \frac{2 \left(\frac{42 \times 10^{-6}}{206265} \right) (16.8 \times 10^6 \times 3.086 \times 10^{16})}{6} \tag{32}$$

Finally, converting this mass into solar masses by dividing by $\frac{GM_\odot}{c^2}$, where $M_\odot$ is the mass of the Sun in kilograms, we estimate the mass of M87*:

$$M \approx \frac{D}{6GM_\odot/c^2} M_\odot \tag{33}$$

This rough estimation, while simplified yields a mass consistent with the value measured by the EHT, $(6.5 \pm 0.7) \times 10^9 M_\odot$, within the margins of observational uncertainties.

The asymmetry in brightness observed in the emission ring, with a significant brightness contrast and a deviation from circularity at a ratio of less than 4:3, suggests a plasma rotating at relativistic speeds close to the black hole. This is known as relativistic beaming. Material rotating in the clockwise direction as seen by the observer, i.e., the bottom part of the emission region is moving toward the observer.

EHT observations are interpreted through the lens of general-relativistic magnetohydrodynamic (GRMHD) models that describe a hot, magnetized accretion disk around a Kerr black hole, which naturally produces a jet. The simulations allow for the parameterization of the black hole spin $a*$ and the dimensionless magnetic flux threading the event horizon, providing a rich framework to describe the observed image features.

The physical parameters and the dynamics of the accretion flow are further encapsulated by GRMHD simulations, which scale with the mass of the black hole. A typical simulation is characterized by the dimensionless spin $a* = Jc/GM^2$, where J and M

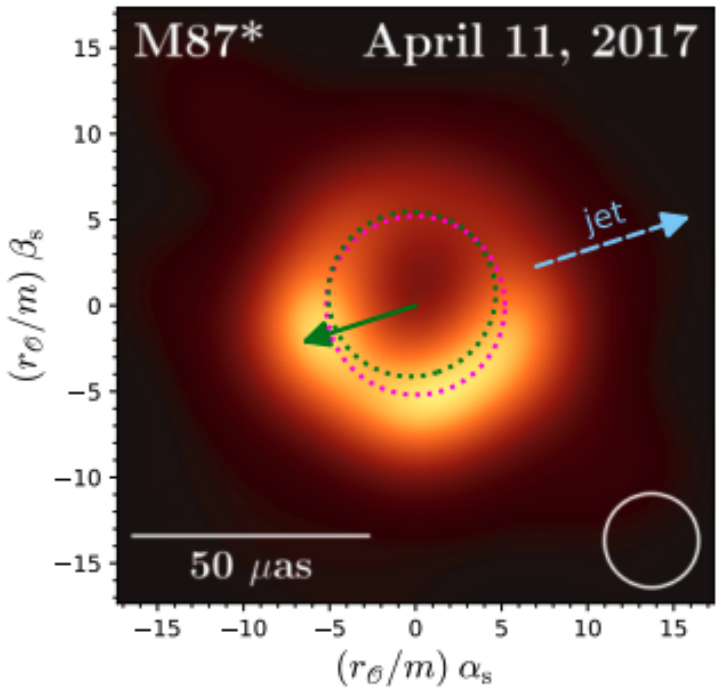

Figure 11: Image of the immediate vicinity of the supermassive black hole M87*, as released by the EHT collaboration in 2019, with two critical curves superposed: that of a Schwarzschild black hole (magenta dotted circle) and that of an extremal Kerr black hole seen under the inclination $\theta_o = 163^o$ (green dotted curve), with the projection of the spin axis onto the screen indicated by the green arrow (position angle $\theta = 108^o$ with respect to the βs-axis)(Credit: Éric Gourgoulhon).

represent the black hole's spin angular momentum and mass, respectively. These simulations contribute to a comprehensive library of synthetic images, used to create model visibilities that match the EHT observations.

3.2 Properties of Sag A*

Astrophysical observations of Sagittarius A* (Sgr A*), the supermassive black hole at the center of our Galaxy, have significantly enhanced our understanding of its properties. The Kerr metric, which characterizes stationary, vacuum, and axisymmetric black holes free of electromagnetic charge, is expected to describe such black holes. The Event Horizon Telescope (EHT) has provided new constraints on the deviations from the Kerr prediction based on 2017 observations of Sgr A* (Akiyama et al., 2022).

The following parameters characterize the black hole Sgr A*:

- Mass (M): The mass of Sgr A* is a crucial parameter, which has been inferred from the dynamics of the central stellar cluster and precisely measured through infrared observations of stars orbiting the black hole. The EHT Collaboration adopts a mass of $M = 4.1 \times 10^6 M_\odot$, which has been determined with high precision from these dynamical measurements.

- Distance (D): Sgr A* is located at a distance of approximately 8 kpc from Earth. This distance has been refined over the years through observations and modeling

of the orbits of stars in the Galactic center.

- Spin (a): The spin of Sgr A* is described by the dimensionless parameter $a = J/M$, where J is the angular momentum of the black hole. The spin determines the innermost stable circular orbit (ISCO) and affects the space-time structure near the event horizon. Based on the reconstruction of dark spots in the images of supermassive black holes SgrA* and M87* provided by the Event Horizon Telescope (EHT) collaboration, the inferred spins for these black holes are determined. The accretion disk model, as well as recent general relativistic magnetohydrodynamic (GRMHD) simulations, support the presence of hot accretion matter in the vicinity of the event horizons of these black holes. This allows for the modeling of the dark spot as a lensed image of the event horizon globe, which can then be used to estimate the spin parameter of the black hole.

  For SgrA*, the spin parameter a, which is defined as the black hole's angular momentum per unit mass, has been inferred to be in the range $0.65 < a < 0.9$. This estimation is based on the size of the dark spot compared to the expected position of the classical black hole shadow. The spin parameter is a crucial characteristic as it influences the radius of the ISCO, the shape of the black hole's shadow, and the dynamics of the accretion disk and relativistic jets.

  The precision of the spin estimation is acknowledged to be at the 1σ confidence level, suggesting that there is room for refinement with future observations and advancements in the EHT or other observatories such as the proposed Millimetron Space Observatory. These observations have the potential to provide sharper images, which could lead to more accurate determinations of the black hole's spin and other parameters.

- Angular Size (θ_g) and Shadow Diameter: The angular size, θ_g, is a crucial observable, representing the apparent size of the black hole's event horizon from our vantage point on Earth. It is defined mathematically as:

$$\theta_g = \frac{GM}{Dc^2} \tag{34}$$

  where G is the gravitational constant, M is the mass of Sgr A*, D is the distance to Sgr A*, and c is the speed of light.

  The shadow cast by Sgr A* is directly related to its mass and the geometry of spacetime in its vicinity. The shadow diameter for a Schwarzschild black hole can be estimated by:

$$d_{\mathrm{sh,Sch}} = \frac{5.2GM}{c^2} \tag{35}$$

  However, for a Kerr black hole like Sgr A*, the diameter is influenced by the spin parameter a, leading to:

$$\hat{d}_m = \alpha_c \left(d_{\mathrm{sh}} + \delta d_{\mathrm{sh,Sch}}\right) \tag{36}$$

  where α_c is the calibration factor accounting for observational and theoretical biases, d_{sh} is the actual shadow diameter, and δ quantifies the deviation from the Schwarzschild case.

  The EHT observations have provided measurements of Sgr A*'s shadow diameter to be approximately 47-50 microarcseconds (μas), which are consistent with the Kerr metric predictions when the black hole's spin is taken into account.

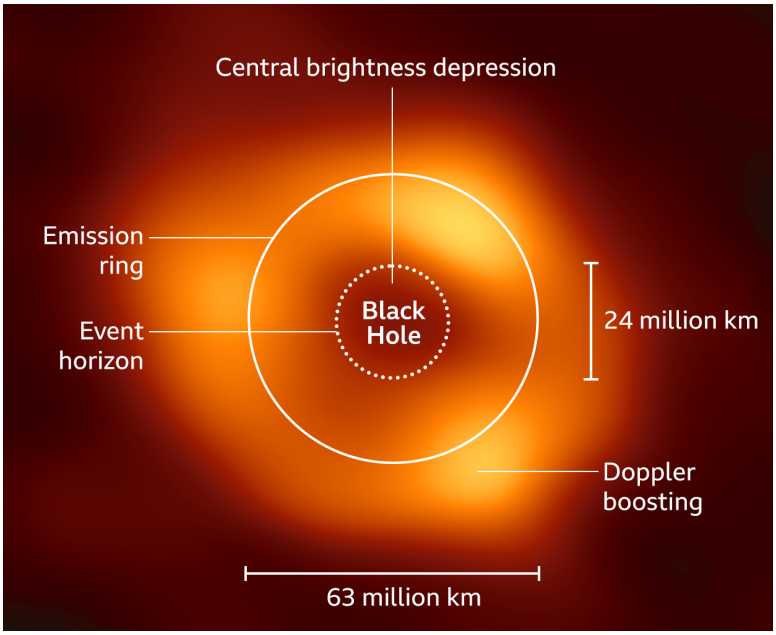

Figure 12: The observed image of Sagittarius A* (Sgr A*), as captured by the Event Horizon Telescope (EHT). Prominent features include the bright emission ring surrounding the central darkness, which is the black hole's shadow against the backdrop of glowing gas. The asymmetry in brightness, attributed to Doppler boosting, indicates the relativistic motion of the emitting material. The scale is given by the diameter of the shadow, approximately 24 million km across, set within the larger context of the surrounding accretion flow with a spatial extent of about 63 million km.

These measurements not only support the existence of Sgr A* as a Kerr black hole but also allow us to probe the nature of gravity in one of the most extreme environments in the universe.

4 The future of VLBI: Quest for sharper shadows

4.1 Current limitations with EHT

EHT utilizes the technique of Very Long Baseline Interferometry (VLBI), which synergistically combines telescopes across the Earth to form a virtual observatory of planetary scale, capable of resolving the shadow of a black hole with remarkable precision.

The angular resolution θ achievable through VLBI is delineated by the relation:

$$\theta \approx \frac{\lambda}{B} \tag{37}$$

where λ is the wavelength of observation, and B is the baseline or the maximum separation between array elements. The EHT, operating at a frequency of 230 GHz – corresponding to millimeter wavelengths – effectively utilizes the Earth's diameter as its baseline, thereby achieving an angular resolution on the order of ~ 22 microarcseconds (μas). This fine resolution has enabled the EHT to observe the shadow of M87*, an image that not only aligns with theoretical predictions but also serves as a crucial test for Einstein's theory of General Relativity.

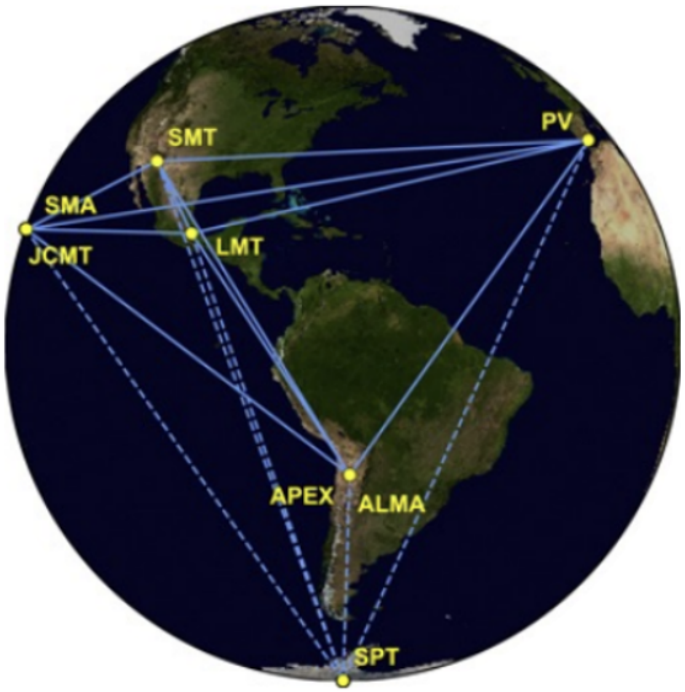

Figure 13: Image showing all the telescopes that were used for EHT observations (Akiyama et al., 2022).

However, EHT's capability is inherently bound by certain limitations. Baselines are limited by the Earth's diameter, and without orbital telescopes, cannot be extended further. Moreover, the Earth's atmosphere presents a formidable barrier; it absorbs significant amounts of incoming millimeter and sub-millimeter radiation, thereby limiting the ground-based observatories to frequencies below 230 GHz. This absorption poses a substantial impediment to capturing the faint signals that emanate from cosmic sources.

Addressing these challenges may involve deploying space-based VLBI stations, which would allow for an unprecedented extension of baseline lengths beyond Earth's confines, and, in turn, significantly refine the angular resolution. Or, balloon-based mobile VLBI stations can also allow observations at higher frequencies as they fly 99.5% above the Earth's atmosphere as shown in Fig 14. Balloons can also help us fill in the $u - v$ space thereby increasing the overall sensitivity of observation.

4.2 Resolving photon rings with ngEHT

In the strong gravitational field near a black hole, light can be bent and captured into orbit, forming what are known as photon rings. These rings are a set of nested, thin rings around the black hole's shadow, each corresponding to photons that have completed an increasing number of half-orbits around the black hole. Specifically, the $n = 0$ photon ring refers to the direct emission that travels from the source to the observer without any orbit, while $n = 1$ and $n = 2$ photon rings consist of photons that have completed one and two half-orbits respectively, with each successive ring becoming fainter and closer to the black hole.

The mathematical description of these rings can be approached by considering the

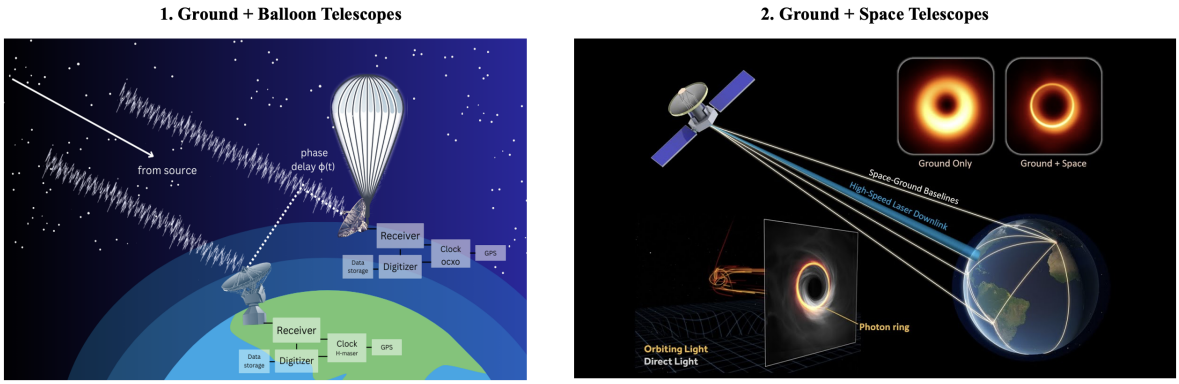

Figure 14: Figure showing the two possible cases of improving the resolution for next-generation VLBI observations. The first image shows how a balloon-borne telescope can be used. The second image shows how space-based VLBI can help us resolve photon rings of nearby black holes.

effective potential V_{eff} for photon orbits in Schwarzschild spacetime, given by:

$$V_{\text{eff}}(r) = \left(1 - \frac{2GM}{c^2 r}\right)\left(\frac{L^2}{r^2} - \frac{G^2 M^2}{c^2}\right), \tag{38}$$

where r is the radial coordinate, M the mass of the black hole, L the angular momentum of the photon, G the gravitational constant, and c the speed of light. This potential describes the gravitational well affecting the photon trajectories.

The next-generation Event Horizon Telescope (ngEHT) seeks to improve upon the current EHT's observations by providing higher-resolution images of these photon rings. The ngEHT is designed to achieve this through enhancements in baseline coverage, frequency bands, and sensitivity. It aims to resolve the $n = 1$ ring, which is anticipated to provide critical information about the black hole's properties and the nature of gravity in extreme environments.

With its increased capabilities, the ngEHT will enhance the visibility amplitude measurements, essential for resolving the fine structure of the photon rings. The visibility amplitude V in the context of VLBI is given by the Fourier transform of the intensity distribution $I(x, y)$:

$$V(u, v) = \int\int I(x, y) e^{-2\pi i(ux+vy)}\, dx\, dy, \tag{39}$$

where (u, v) represents the spatial frequencies corresponding to the interferometric baselines. By extending these baselines and observing at higher frequencies, the ngEHT will be able to discern the details of the photon rings with unprecedented clarity, offering new insights into the physics of black holes and testing the predictions of General Relativity in the strong-field regime.

5 Conclusion

The Kerr metric has profoundly influenced our conception of rotating black holes and the fabric of spacetime. It describes a rotating black hole's gravitational field and the subsequent behavior of matter and light near it. Through the predictions of the Kerr metric,

such as the distinct shadow and photon rings, we've begun to unravel and characterize our observations of black holes.

Very Long Baseline Interferometry (VLBI) has translated these theoretical predictions into empirical scrutiny. The Event Horizon Telescope, an exemplary VLBI network, achieved a scientific milestone by capturing the shadow of M87*, confirming the Kerr metric's predictions, and reinforcing the theory of General Relativity under extreme conditions. Despite these advances, the quest for sharper shadows persists. The next-generation Event Horizon Telescope (ngEHT) and VLBI experiments promise to expand upon current capabilities. By offering enhanced baseline coverage and sensitivity, they will enable more detailed observations of the photon rings that cloak black holes. The use of space-based and balloon-borne VLBI stations will play a crucial role in this.

References

Kazunori Akiyama, Antxon Alberdi, Walter Alef, Juan Carlos Algaba, Richard Anantua, Keiichi Asada, Rebecca Azulay, Uwe Bach, Anne-Kathrin Baczko, David Ball, et al. First sagittarius a* event horizon telescope results. i. the shadow of the supermassive black hole in the center of the milky way. *The Astrophysical Journal Letters*, 930(2): L12, 2022.

Roger D Blandford and Roman L Znajek. Electromagnetic extraction of energy from kerr black holes. *Monthly Notices of the Royal Astronomical Society*, 179(3):433–456, 1977.

Event Horizon Telescope Collaboration, K Akiyama, A Alberdi, W Alef, K Asada, R Azuly, et al. First m87 event horizon telescope results. i. the shadow of the supermassive black hole. *Astrophys. J. Lett*, 875(1):L1, 2019.

Albert Einstein et al. The foundation of the general theory of relativity. *Annalen Phys*, 49(7):769–822, 1916.

EinsteinPy Development Team. *EinsteinPy: A Python library for General Relativity*, 2024. URL `https://einsteinpy.org/`.

Elena Gallo, Rob Fender, Christian Kaiser, David Russell, Raffaella Morganti, Tom Oosterloo, and Sebastian Heinz. A dark jet dominates the power output of the stellar black hole cygnus x-1. *Nature*, 436(7052):819–821, August 2005. ISSN 1476-4687. doi: 10.1038/nature03879. URL `http://dx.doi.org/10.1038/nature03879`.

Roy P Kerr. Gravitational field of a spinning mass as an example of algebraically special metrics. *Physical review letters*, 11(5):237, 1963.

JM Miller. Relativistic x-ray lines from the inner accretion disks around black holes. *Annu. Rev. Astron. Astrophys.*, 45:441–479, 2007.